Instrumentation for in situ flow electrochemical Scanning Transmission X-ray Microscopy (STXM)

Vinod Prabu, Martin Obst, Hooman Hosseinkhannazer, Matthew Reynolds, Scott Rosendahl, Jian Wang, and Adam P. Hitchcock

Citation: Review of Scientific Instruments **89**, 063702 (2018); doi: 10.1063/1.5023288
View online: https://doi.org/10.1063/1.5023288
View Table of Contents: http://aip.scitation.org/toc/rsi/89/6
Published by the American Institute of Physics

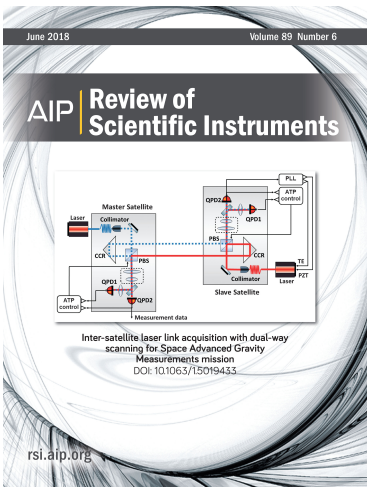

Instrumentation for *in situ* flow electrochemical Scanning Transmission X-ray Microscopy (STXM)

Vinod Prabu,[1] Martin Obst,[2] Hooman Hosseinkhannazer,[3] Matthew Reynolds,[3] Scott Rosendahl,[4] Jian Wang,[4] and Adam P. Hitchcock[1,a)]
[1]*Department of Chemistry and Chemical Biology, McMaster University, Hamilton, Ontario L8S4M1, Canada*
[2]*BayCEER, University of Bayreuth, D-95448 Bayreuth, Germany*
[3]*Norcada, Inc., Edmonton, Alberta T6E5B6, Canada*
[4]*Canadian Light Source, 44 Innovation Boulevard, Saskatoon, Saskatchewan S7N 2V3, Canada*

(Received 23 January 2018; accepted 11 May 2018; published online 7 June 2018)

We report the design and performance of a 3-electrode device for real time *in situ* scanning transmission X-ray microscopy studies of electrochemical processes under both static (sealed, non-flow) conditions and with a continuous flow of electrolytes. The device was made using a combination of silicon microfabrication and 3D printing technologies. The performance is illustrated by results of a study of copper deposition and stripping at a gold working electrode. X-ray absorption spectromicroscopy at the Cu 2p edge was used to follow the evolution as a function of potential and time of the spatial distributions of Cu(0) and Cu(I) species electro-deposited from an aqueous solution of copper sulphate. The results are interpreted in terms of competing mechanisms for the reduction of Cu(II). *Published by AIP Publishing.* https://doi.org/10.1063/1.5023288

I. INTRODUCTION

Electrochemistry is widely applied in many fields, such as the manufacturing of integrated circuits,[1] bio-sensors,[2] solar cells,[3] fuel cells,[4] energy storage devices,[5] and conformal metal coatings.[6] There are strong interests in how the nanostructure may influence electrochemistry and how the optimization of an electrochemical process can play a role in the synthesis of nanostructures.[7–10] Electrochemistry at the macro-scale is well developed.[11] However, electrochemistry at micro- or nano-scales behaves rather differently,[12–15] especially when the rate of arrival of electrochemical reagents at electrodes is diffusion limited.[16] *In situ* spectroscopy techniques[17] can be a powerful tool to probe the chemical states of an electrochemical system under active potential control. If they can be detected, the identification and quantitation of metastable or reactive intermediates can provide key insights into reaction mechanisms. Typically, these are best detected through *in situ* experiments. However, *in situ* experiments are very challenging. If the phenomena of interest are localized at the micro- or nano-scale, the measurements must be performed in some type of analytical microscope—so-called spectro-electrochemical microscopy.[18–20] In addition to electron microscopy-based methods which are described below, there are a variety of absorption, transmission, and reflectance spectro-microscopies, including *in situ* UV-VIS spectro-electrochemistry, to study optically differentiated charge carriers during redox transformation,[21] *in situ* FT-IR and Raman spectroscopy to probe electrochemical changes in chemical bonds,[22] *in situ* Electron Spin Resonance (ESR) spectroscopy for the characterization of radical anions and cations in the electrochemical double layer region,[23] *in situ* NMR spectroscopy for the investigation and characterization of electro-organic reactions,[24] etc. Often, these *in situ* techniques are used in combination with conventional electrochemical characterization techniques such as electrochemical impedance spectroscopy and AC conductance studies.[11] On similar lines, the development of *in situ* soft X-ray, microscopy, with *in situ* flow capability to change the electrolyte, would enable experimenters to investigate electrochemical processes with chemical sensitivity (X-ray absorption spectra) and high spatial resolution (~25 nm). A successful spectro-electrochemical microscopy requires adequate chemical sensitivity to the sample system of interest, electrical contacts, the presence of a suitable electrolyte (often aqueous), and, if possible, a reference electrode.[25,26]

We are developing *in situ* electrochemical instrumentation and methods for soft X-ray Scanning Transmission X-ray Microscopy (STXM). The STXM provides chemical speciation and quantitative analysis at a spatial resolution of ~25 nm.[27] The spectroscopic basis of STXM is near edge X-ray absorption spectroscopy (NEXAFS).[28] In 2005, our group first demonstrated *in situ* soft X-ray STXM electrochemical capabilities.[29] Since then it has been extensively developed and exploited by Bozzini and co-workers[30–32] for a range of systems and, more recently, by several groups for *in situ* and *operando* studies of lithium batteries[33–35] and for metal deposition.[36,37] However, *in situ* electrochemical-STXM experiments are still very challenging due to the large attenuation coefficients of soft X-rays and the very short focal length of the soft X-ray STXM. Improvements in instrumentation and methods are needed. In the hard X-ray region (>2 keV), *in situ* electrochemical studies using spectroscopy[38,39] and spectromicroscopy[40] are quite well developed since the constraints in terms of the sample thickness and cell dimensions are much less severe.

In situ studies of electrochemical processes using transmission electron microscopy (TEM) have become

a)Author to whom correspondence should be addressed: aph@mcmaster.ca. Telephone: 905 525-9140.

popular recently, stimulated in large part by the availability of reliable commercial instrumentation. Although there were earlier attempts,[41–43] the first *in situ* electrochemical studies using the modern TEM were reported by Williamson *et al.* in 2003.[44] In recent years, many groups have applied *in situ* electrochemical electron microscopy techniques to study metal deposition,[18,45–47] Li battery systems,[48,49] fuel cells,[50] and other systems.[51] The *in situ* electrochemical TEM is very powerful since it combines very high (sub-nm) spatial resolution and rapid data collection, including real time imaging.[52] There are cases where spectroscopic methods—specifically energy dispersive X-ray spectroscopy (EDS)—have been used to perform local elemental analysis in the *in situ* electrochemical TEM.[53] However, the thick fluid media of an electrochemical cell cause extensive multiple scattering,[49] which makes it difficult to perform core level electron energy loss spectroscopy (EELS), which is the only TEM-based analytical method providing information on oxidation states and chemical speciation. Although spatial resolution (~25 nm) is worse and data acquisition speed (~10-30 s/image) is slower in the STXM compared to the TEM, the ability to perform high quality X-ray absorption spectroscopy for the identification of chemical species provides a strong motivation for the development and application of *in situ* electrochemical soft X-ray STXM. Our ultimate goal is to provide STXM instrumentation platforms similar to those for *in situ* electrochemical TEM for applications in many areas including energy materials, environmental sciences, and soft matter research.

Previously, we demonstrated the *in situ* electrochemical-STXM under sealed, non-flow conditions in a study of electrochromism in electrodeposited polyaniline.[29] More recently, we have reported preliminary results on the role of electrolyte pH in determining the chemical species present in copper electro-deposition and stripping.[54] The *in situ* system used for that Cu study, which was phase 1 of this instrument development project, was only capable of operating with a sealed cell. However, for *in situ* X-ray spectro-electrochemical studies, it is advantageous to be able to flow electrolytes and reagents into and out of the *in situ* cell. An instrument capable of flow electrochemical studies allows an experimenter to perform electrochemical studies under kinetic growth conditions through continuous replenishment of the electroactive species. It also provides the ability to change the electrolyte, to control pH, or to change concentrations of reactive species (within the scope of the system under study) rather than setting up a whole new device.

This paper reports our recent progress toward the development of a reliable and cost-efficient system to perform *in situ* flow electrochemical STXM studies. This consists of custom micro-fabricated silicon chips having X-ray transparent silicon nitride windows with lithographically deposited electrodes, which are combined with a novel 3D printed sample holder with provision for the flow of the electrolyte and mounting in the STXM using a common 3-pin kinematic mounting scheme.[55] The performance of the current device (referred to as phase 1b) as a tool to investigate electrochemical changes at electrode-electrolyte interfaces is evaluated through an *in situ* flow electrochemical STXM study of copper electro-deposition and electro-stripping at the gold working electrode.

II. INSTRUMENTATION

A. Silicon chip device: Design and fabrication

Figure 1 presents details of the phase 1b silicon device for the *in situ* flow electrochemical STXM developed by the academic authors in collaboration with Norcada, Inc. Two custom silicon chips were fabricated: one with electrodes (chip "E") and the other with a channel defined by a spacer (chip "F"). The electrode chip "E" [Fig. 1(a)] is 12 mm × 5 mm in size, 200 μm thick silicon with 3 gold electrodes, which are at a mm scale on most of the chips and reduce in size to μm scale on the 100 nm thin, X-ray transparent silicon nitride membrane window of size 200 μm × 80 μm. The entire surface of chip "E," except the window and small areas around the window (270 μm × 150 μm) and the electrical contact pad of the electrodes at the top (5 mm × 2.5 mm), is coated with an electrically insulating passivation layer to ensure that almost all the observed electrical signals come from the window area where STXM studies can be performed. Two square inlet and outlet ports (0.8 mm × 0.8 mm), placed with vertical offsets, are etched through electrode chip "E" to allow provision for the continuous or intermittent flow of the liquid electrolyte.

Figure 1(d) is an expanded view of the window region, showing the detailed design of the active region of the electrodes. The hemispherical electrode at the top is used as the working electrode (WE). The large electrode on the right is used as the counter electrode (CE). The third, narrow electrode, to the left of the WE, is used as the reference electrode (RE). Together they form a three-electrode cell system. The electrode design differs from designs in analogous planar devices for *in situ* electrochemistry, which typically have the counter electrode surrounded by a circular working electrode.[33,56] Our design was chosen in order to have a sufficient area on the WE for ink-jet printing a structure similar to the cathode in a polymer electrolyte membrane fuel cell (PEM-FC), a future goal of this project. Another reason for this choice of electrode design is to minimize the chance of shorting the CE and WE by electrodeposited dendrites. The darker circles on the WE and the CE are regions with a much thinner Au coating to allow studies on an area where there is no edge-enhanced field and where the electrode absorption is sufficiently small to allow studies at the C 1s edge.

The spacer chip "F" [Fig. 1(b)] is 9 mm × 5 mm in size, 200 μm thick silicon and has a 240 μm × 120 μm, 50 nm thin X-ray transparent Si_3N_4 window, fabricated using Norcada proprietary hydrophilic SiNx. Most of the surfaces of chip "F" are coated with a 1.5 μm thick, non-polymeric, insulating, hydrophobic spacer layer, leaving a hydrophilic "J" shaped flow channel. The tops of the "J" channels align with the two flow ports on the electrode chip, "E," and arcs around the window on the spacer chip. This "J" channel defines the path for the liquid electrolyte to flow to and over the window region. The hydrophilic character of SiN_x used facilitates the flow of the aqueous electrolyte within the channel. Figure 1(c)

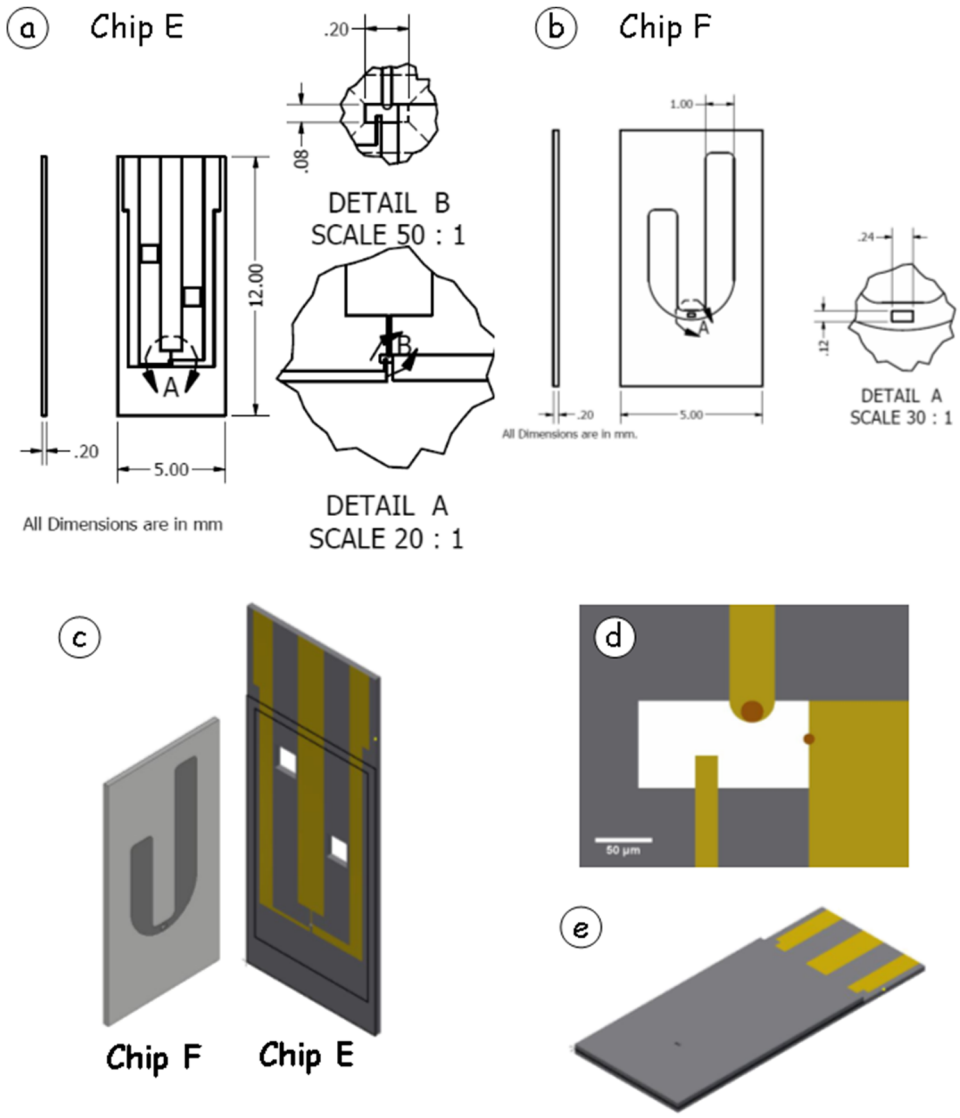

FIG. 1. Design of silicon/silicon nitride chips for use in *in situ* flow electrochemistry STXM studies. (a) Electrode chip "E." (b) Spacer chip "F." (c) Cartoons of the electrode and spacer chip. (d) Expanded view of the soft X-ray transparent silicon nitride window and electrodes. (e) Cartoon of the assembled device.

contains images from the CAD models of the electrode and spacer chip. The idea is to enclose a 1.0–1.5 μm thin film of the liquid electrolyte between the two chips. After assembling the electrode chip as the downstream chip and the spacer chip as the upstream chip, a complete, but unsealed, cell is formed [Fig. 1(e)].

B. Sample holder design and fabrication

An *in situ* flow electrochemical cell holder (called the phase 1b holder) was designed and fabricated using a Projet® 3510 SD multi-jet 3D printer. Its functions include supporting the assembled electrode chips, attaching the system to the 3-pin STXM kinematic mount,[54] hermetic (liquid-tight) sealing the sandwich of electrode-spacer chips, connecting to the fluid flow, and establishing electrical biasing. The holder consists of three pieces: the base [Fig. 2(a)], the keeper [Fig. 2(b)], and the bias [Fig. 2(c)]. These parts were 3D printed using a UV curable acrylic polymer (Visijet M3 crystals). The acrylic polymer is a semi-solid gel in its uncured form. After UV exposure and curing, it does not contain any voids, which minimizes outgassing under high vacuum conditions.[57]

The sides of the base piece have thin, uniform areas (fins) with smooth edges, which are sized to slide into the 3-pin kinematic mounting scheme used in many soft X-ray STXMs.[55] The base has two ports on the top, which mate with flangeless microfluidic fittings (Idex model M660)[58] that are used to connect the device to a syringe pump (New Era Syringe Pump, NE1010)[59] through ethylene tetrafluoroethylene (ETFE) tubing (Idex model Tefzel^{TM}1517).[58] The syringe pump is used in the infusion mode in order to maintain a stable, low rate flow of fluid into the STXM *in situ* cell. The base piece has a 400 μm deep rectangular slot [Fig. 2(a)] into which the assembled silicon chips "E" and "F" are placed. The surface of the rectangular housing has two hollow frustum shaped features [Figs. 2(d)–2(f)], which align and plug into the flow ports on the electrode chip. These features are surrounded by grooves to house O-rings[60] (1.5 mm diameter $\times$ 0.45 mm width) which seal between the holder and the flow ports on the electrode chip. The keeper piece is designed to hold the two chips in place when the holder is mounted vertically in the 3-pin mount in an oxygen-free helium environment. 00-80 NCF stainless steel (SS) screws are used to apply a gentle pressure on the O-rings in order to seal the flow channel.

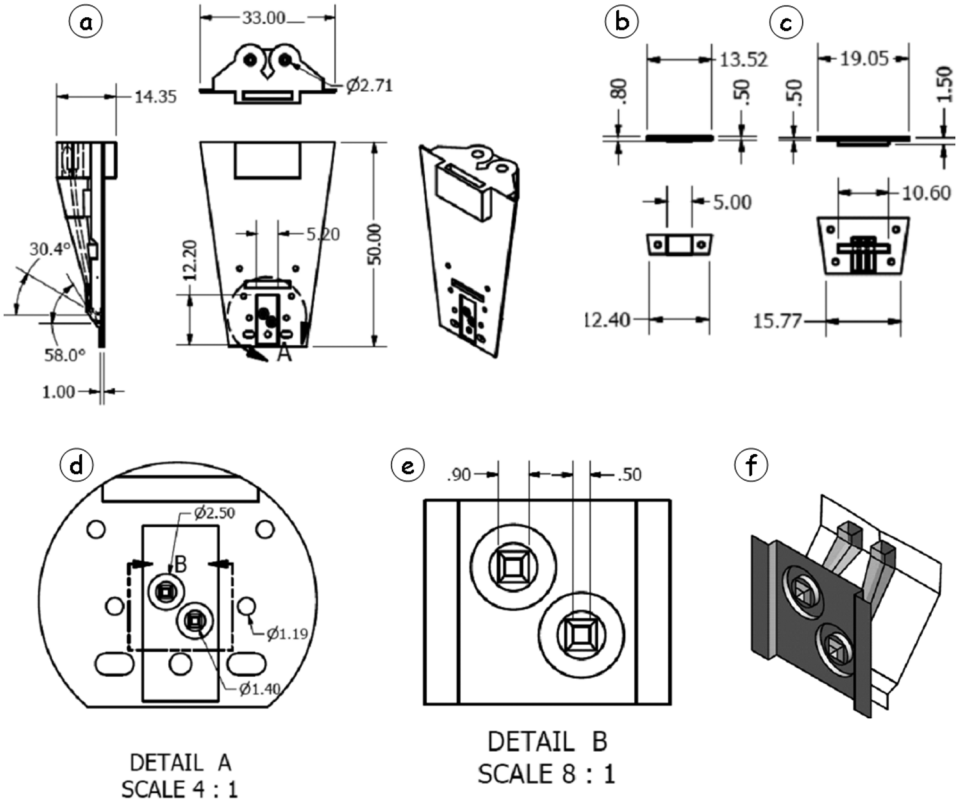

FIG. 2. Design of the *in situ* flow cell 3D printed holder. (a) Overall design of all components. (b) Design of the keeper piece. (c) Design of the biasing piece. [(d) and (e)] Detail of o-ring sealed flow ports. (f) Isometric view of detail B (e).

The initial hope was that the pressure exerted by the keeper piece on the pair of chips would provide a vacuum-tight seal using the hydrophobic spacer coating as a gasket. However, when assembled and tested under high vacuum, there were leaks at the interface between the electrode and spacer chips, so the present work was conducted under a static 1 bar of helium gas, achieved by flowing He through the STXM chamber for ~15 min to displace the air. The absence of a pressure differential meant there was negligible leak of the electrolyte from the cell into the STXM chamber.

The bias piece is equipped with three copper electrical contact strips of 10 × 1 mm dimensions, which slide into 3 parallel slots on the bias piece. These strips make contact with the Au electrodes on chip "E" and are fixed in position using 00-80 NCF screws to attach to the insulating polyacrylate body of the holder. This provides an independent electrical connection of the 3 electrodes on the window to a potentiostat (Ivium Pocketstat)[61] located outside the STXM. The electrical interface through the STXM chamber wall uses standard Bayonet Neill-Concelman (BNC) connectors at ambient-STXM at the Canadian Light Source (CLS) and SubMiniature version A (SMA) connectors at STXM 11.0.2 at the Advanced Light Source (ALS).

Figure 3(a) (Multimedia view) presents an exploded view of the assembled *in situ* flow cell on the holder. Figure 3(b) (Multimedia view) is a photograph of an assembled device ready to mount in the STXM. So far, this device has been tested for compatibility and used with STXM instrumentation at PolLux-X07DA at the Swiss Light Source (Switzerland), with STXM 11.0.2 at the Advanced Light Source (Berkeley, California, USA), and at the ambient-STXM on beamline 10ID-1 at the Canadian Light Source (Saskatoon, Canada).

III. EXPERIMENTAL METHODS

A. Sample materials

The Cu 2p reference spectra for Cu(I) and Cu(II) species were obtained from an *ex situ* sample prepared on a two electrode silicon chip by constant current electrodeposition on Au from an electrolyte of 0.1M $CuCl_2 \cdot 2H_2O$ (reagent grade, ≥99%, Sigma-Aldrich) in milli-Q water (≤20 ppm) for 2 min (min). This resulted in finely segregated species of Cu(I) and Cu(0), and some amount of precipitated $CuCl_2$ salt on the window surface due to inadequate washing post electro-deposition. A copper metal [Cu(0)] reference sample was prepared by electrodeposition at −0.5 V for 20 s from an electrolyte of 10 mM $CuSO_4$ in 0.1M H_2SO_4 solution, on the Au electrodes of two electrode silicon chips. The chemicals used for the *in situ* flow study were cupric sulphate pentahydrate ($CuSO_4 \cdot 5H_2O$, reagent grade, Sigma-Aldrich, ≥98%), ammonium sulfate [$(NH_4)_2SO_4$, reagent grade, Sigma-Aldrich ≥98%], and sulphuric acid (H_2SO_4, reagent grade, Sigma-Aldrich, 95%-98%).

B. Scanning Transmission X-ray Microscopy (STXM)

The results reported in this paper were measured using the ambient-STXM on CLS beamline 10ID1.[62] The instrumentation, typical imaging techniques, and analytical spectromicroscopy methods have been described elsewhere.[27] In brief, the sample is raster scanned at the focus of a Fresnel zone plate while synchronously measuring the transmitted, monochromatic X-ray flux. Image sequences at a series of photon energies (also referred to as stacks[63]) are recorded for subsequent detailed analysis. Point spectra, single images,

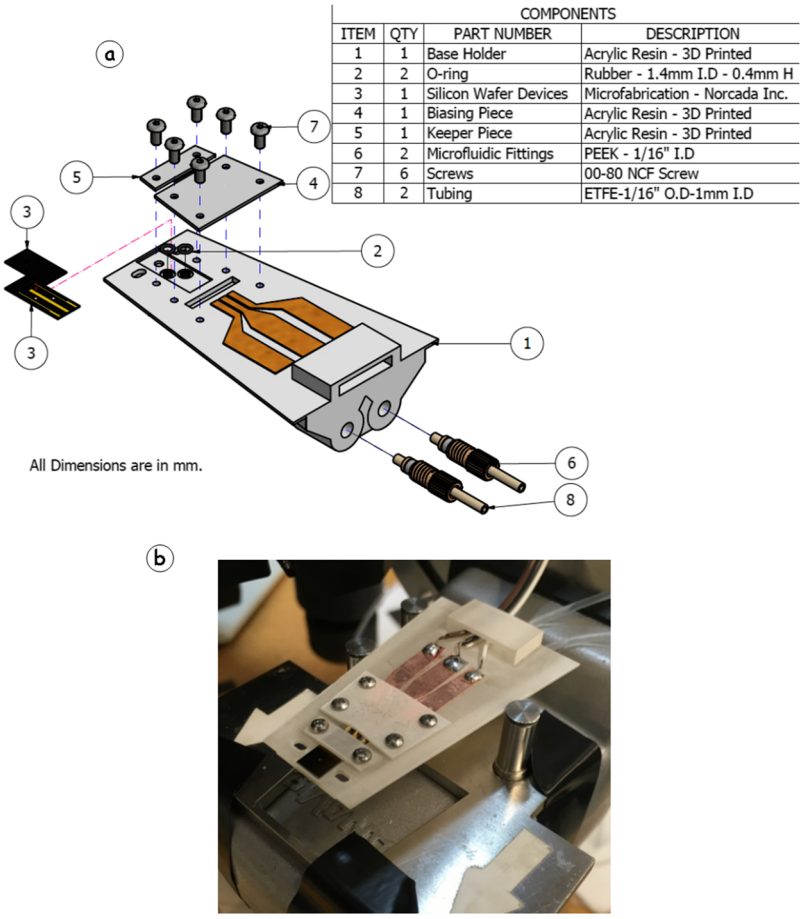

COMPONENTS

ITEM	QTY	PART NUMBER	DESCRIPTION
1	1	Base Holder	Acrylic Resin - 3D Printed
2	2	O-ring	Rubber - 1.4mm I.D - 0.4mm H
3	1	Silicon Wafer Devices	Microfabrication - Norcada Inc.
4	1	Biasing Piece	Acrylic Resin - 3D Printed
5	1	Keeper Piece	Acrylic Resin - 3D Printed
6	2	Microfluidic Fittings	PEEK - 1/16" I.D
7	6	Screws	00-80 NCF Screw
8	2	Tubing	ETFE-1/16" O.D-1mm I.D

FIG. 3. (a) Cartoon showing the assembly of the *in situ* flow cell on the 3D-printed holder. This is a frame from an animation of the assembly procedure. (b) Photograph of a completely assembled device ready to mount into the STXM. Multimedia view: https://doi.org/10.1063/1.5023288.1

line scan spectra, or few-image stacks are used, coordinated with continuous or step changes in the cell potential in order to follow electrochemically induced changes to the system.

As-measured transmission images are converted to optical density (OD) images through the Beer-Lambert Law, $OD = \log(I_0/I)$, where I_0 is the incident photon flux, which can be measured either through a hole in the phase 1b holder or through an area of the silicon nitride windows of the cell where there is only electrolyte, and I is the photon flux transmitted through the sample area of interest. aXis2000[64] was used for stack alignment, conversion to OD, and generation of chemical maps from the *in situ* data. The spectra of Cu(0), Cu(I), and Cu(II) oxidation states, recorded separately from the pure materials, were converted to the optical density per nanometer thickness (OD1) intensity scale[27] by scaling the measured OD outside the near edge structured region to match the elemental OD1 computed from the tabulated elemental cross sections,[65] the elemental composition, and the material densities (8.94 g cm^{-3}, 6.00 g cm^{-3}, and 6.31 g cm^{-3} for Cu metal,[66] Cu_2O,[67] and CuO,[68] respectively).

C. *In situ* flow cell setup

Successful operation of a microfluidic flow cell requires a minimal dead volume in the system during operation, so the inlet tubing and the outlet tubing are pre-filled with the electrolyte using a syringe fitted with a 0.5 μm rated syringe filter (BD plastic).[69] An *in situ* flow cell was assembled using the phase 1b silicon chip devices. A detailed, illustrated guide to the device assembly procedure is given in the first author's M.Sc. thesis.[70] An animation of the assembly process as an mp4 movie is available as a linked Multimedia view from the electronic version of the paper. A movie showing chemical maps of the changes in Cu chemistry at the working electrode as a function of applied potential over 3 cycles is also provided as a Multimedia view available from the electronic version of the paper.

After the assembly of the device, a flow rate of 24 μl/h was set on the syringe pump and was left under continuous flow for 1 h until a small droplet of the electrolyte was observed at the end of the outlet tubing. The flow rate of 24 μl/h was chosen based on Hagen-Poiseuille calculations for the flow of fluid through a rectangular microfluidic channel, using the dimensions of the J-channel in the flow cell [Eq. (1)],[71]

$$Q = \left[1 - 0.630\frac{h}{w}\right]\frac{h^3 w}{12\eta L}\Delta p, \tag{1}$$

where Q is the flow rate of the electrolyte, h is the height of the spacer layer (1.5 μm), w is the width of the channel (1000 μm), η is the viscosity of the electrolyte, L is the length of the channel (~10 mm), and Δp is the pressure head between the inlet and the outlet flow ports on the chip assembly, which was calculated to be 0.01 bar, based on the average velocity of the fluid flow and equivalent diameter of the microchannel.[72]

Although the X-ray path length from the Si_3N_4 window isolating the STXM tank from the ultrahigh vacuum (UHV) beamline to the detector is only 3-6 mm (the distance depends on photon energy), at atmospheric pressure of air, most of the soft X-ray flux is absorbed by the air before reaching the detector. While it is possible to perform STXM with 1 atm air present at 395 eV (i.e., below the onset of absorption by N_2), it is generally best to replace the air with He for better quality measurements, to access the full spectral range of the beamline and to avoid additional radiation damage from activated oxygen species. In our experience, despite careful tightening of the keeper piece, and even with epoxy sealing, if the STXM is actively pumped to high vacuum, the phase 1b flow cell will leak the electrolyte from the edges of the silicon chip sandwich, i.e., the spacer layer in chip "F" does not act as a gasket. Over the long term, the small residual leak can damage the STXM. Thus, we minimize the amount of the leaked electrolyte by always keeping the pressure at 1 atm. Operationally, the air in the STXM tank is displaced by (i) opening an exit valve and (ii) establishing a slight overpressure of pure He such that there is a low flow of He gas at the exit valve (all other ports on the STXM tank must be fastened with screws to avoid the back flow of air). The time required to replace the air with He depends on the volume of the STXM tank and the overpressure, but it is typically 10-15 min. The progress of air removal can be monitored by measuring the transmitted X-ray signal at 401.1 eV (the peak of the N 1s $\rightarrow \pi^*$ transition in N_2). Once the 401.1 eV signal is saturated, the STXM tank is sealed.

D. *In situ* flow cell electrochemical STXM: Data acquisition and treatment

The STXM acquires data serially, with each pixel in an image measured sequentially. Since the main goal is to visualize electrochemical changes, the acquisition scheme was chosen to allow chemically sensitive measurements as fast as possible. Previously multi-point spectra and line-scan spectral measurements have been used for *in situ* electrochemical studies.[29] In this work, we wished to image electrochemical changes over most of the working electrode so we measured a series of image sequences (stacks), each consisting of 3 discrete energies chosen to visualize and quantify Cu species present over restricted potential ranges during continuous potential scan *in situ* operation. The energies chosen were 930.5 eV (pre-edge background), 933.1 eV [main Cu 2p $\rightarrow$ 4s peaks of Cu(I) and Cu(0), which overlap], and 937.0 eV [first continuum multiple scattering peak of Cu(0), where the ratio of the 933.1–937.0 eV intensities are very different for Cu(0) and Cu(I)]—see Fig. 4. The signals at these three energies are analyzed by fitting the values at each pixel to the OD1 reference spectra (Fig. 4) to generate quantitative component maps of Cu(0) and Cu(I). Although the 930.5 eV signal is where Cu(II) absorbs (see Fig. 4), the amount of Cu^{2+} in the electrolyte is so small that it can be safely ignored, and thus the signal at 930.5 eV is a valid pre-edge measure of the non-Cu intensity, associated with the silicon nitride windows, water, and Au electrodes.

An Ivium Pocketstat potentiostat[61] was used for all electrochemical measurements. The performance of the phase 1b

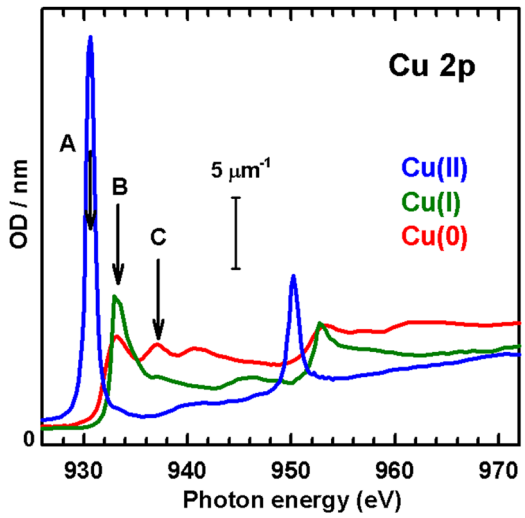

FIG. 4. Cu 2p reference spectra of Cu(0), Cu(1), and Cu(II), measured from electrodeposited Cu metal, CuCl, and $CuCl_2 \cdot 2H_2O$, respectively. The intensity scale is absolute in terms of the OD/nm thickness at standard densities of the solids (OD1). The arrows labeled A, B, C indicate the energies used to determine Cu(0) and Cu(I) amounts in the *in situ* flow electrochemical study.

in situ flow electrochemical STXM was evaluated by probing the spatial distributions of the Cu(0) and Cu(I) species on and beside the working electrode at several potentials during a very slow (5 mV/s) but continuous cyclic voltammetry scan which spanned potentials for both the reduction and oxidation of Cu. Based on our earlier work under static conditions,[54,70] electrodeposition at potentials below −0.3 V (with respect to the Au reference electrode on the device) from a 0.1M H_2SO_4 electrolyte (pH = 1) with less than 0.1M $CuSO_4 \cdot 5H_2O$ yields only copper metal. When the electrodeposition is carried out at higher pH (2.5-4.0) under restricted diffusion conditions, and without an added supporting electrolyte, there is co-deposition of a Cu(I) species (Cu_2O).[70,73] Here an aqueous solution of 5 mM $CuSO_4 \cdot 5H_2O$ in milli-Q water (≤20 ppm) (pH = 4.75) was the electrolyte, and the *in situ* STXM was used to probe the amounts and spatial distributions of Cu(I) and Cu(0) species. In order to increase the ionic conductivity of the electrolyte and to minimize the ohmic (IR) drop, 25 mM $(NH_4)_2SO_4$ was used as a supporting electrolyte. Three cycles of *in situ* cyclic voltammetry (CV) through a potential range of +0.15 to −0.5 V at a sweep rate of 5 mV/s were performed while maintaining an electrolyte flow rate of 24 μl/h. At this flow rate, the volume measured by the STXM (30 μm × 30 μm × 2 μm = 1800 μm^3 or 1.8×10^{-6} μl) is replaced every 0.3 ms, so it is safe to assume that the electrolyte composition, in particular, $[Cu^{2+}]$, was maintained constant throughout the measurement.

The parameters defining the image quality, scan area, step size, and dwell time/pixel were chosen so that the acquisition time for each image was ~20 s. The CV potential scans (scan rate of 5 mV/s over a potential span of 1.3 V, executed automatically over 3 cycles) took 780 s. Thus, during the course of a single *in situ* measurement, 13 stacks were acquired, each containing 3 images. These parameters are a balance between the image size, spatial sampling, chemical sensitivity, and speed of data collection.

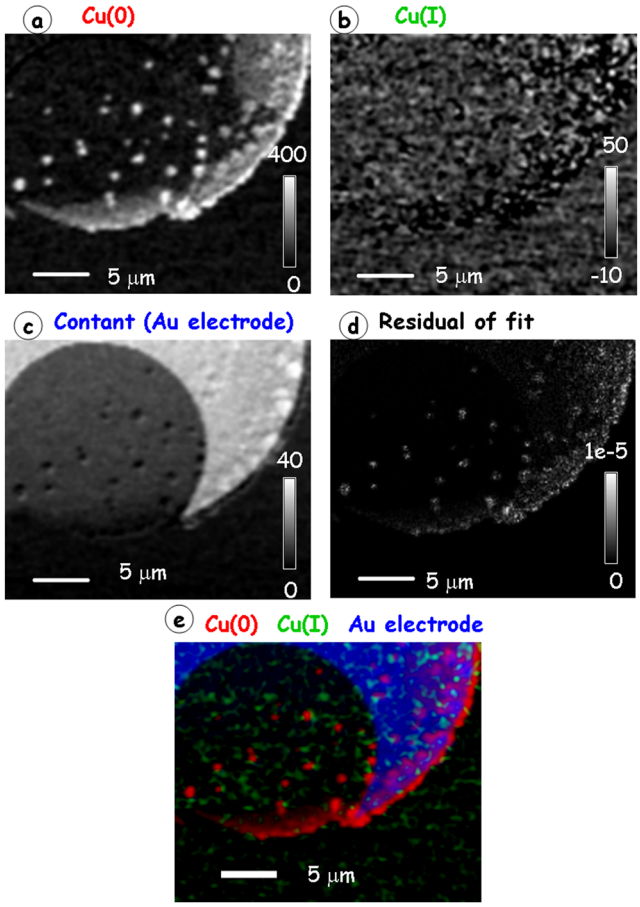

FIG. 5. Component maps for (a) Cu(0), (b) Cu(I) and (c) constant (Au electrode) derived from a singular value decomposition fit of a 3-energy Cu 2p stack during *in-situ* flow electrochemical study. The grayscale units are nm thickness, at standard density. (d) Residual map from the fit (grayscale in units of OD). (e) Rescaled color coded composite map of Cu(0) (red), Cu(I) (green) and Au electrode (blue).

Each 3-energy stack, consisting of OD images (100 × 83 pixels) at 930.6, 933.1, and 937.0 eV, was aligned, converted to optical density and fit using singular value decomposition[74] to the Cu(0) and Cu(I) OD1 reference spectra (Fig. 4), and a constant, representing the Au electrode. An example is presented in Fig. 5 which displays the Cu(I) and Cu(0) and constant component maps and the residual of the fit, as well as a color coded composite. The maps from the *in situ* data are quantitative due to the use of OD1 reference spectra in the fit. Outlier signals in the component maps are removed by histogram clipping, and a color composite map with rescaling is generated using red for Cu(0), green for Cu(I), and blue for constant (the Au electrode). This gives a visual representation of the distribution of Cu(0) and Cu(I) species [Fig. 5(e)]. Threshold masks (map of components on a 0/1 z-scale) were then generated from the Cu(0) and Cu(I) thickness maps in order to derive the average amounts of Cu(I) and Cu(0) at each potential. After multiplying the thickness maps by the threshold masks, the non-zero pixels were averaged to give the average thickness of the Cu(0) and Cu(I) deposits at a given potential in the 3-cycle *in situ* measurement. The resulting average thickness and area information were used to compute the amount (in ng) of each component deposited, through conventional mass-density calculations using standard densities. To evaluate uncertainties, a similar procedure of averaging the thickness data for each species was repeated 3 times.

IV. RESULTS

A. Reference spectra of pure species and speciation strategy

Figure 4 presents the Cu 2p X-ray absorption spectra for Cu metal, CuCl, and $CuCl_2 \cdot 2H_2O$, on an absolute OD1 intensity scale. These spectra are similar to literature spectra of Cu metal,[75] Cu_2O,[74] and CuO[76,77] in terms of shape and energies of the absorption peaks. Energies of the main spectral features in these reference spectra are compared to literature values in Table I. The first strong peak in the Cu $2p_{3/2}$ portion of the 3 spectra occurs at 930.6(2) eV (A), 933.06(8) eV (B), and 933.1(2) eV, for Cu(II), Cu(I), and Cu(0), respectively. For Cu(II), where there is a hole in the 3d band ($[Ar]3d^9$), the strong, sharp peak at 930.6(2) eV is due to Cu $2p_{3/2} \rightarrow$ 3d transitions. The exact position of the $2p_{3/2} \rightarrow$ 3d transition in Cu(II) compounds depends on the local environment. Phillips *et al.*[77] have reported variations of up to 0.8 eV in the Cu $2p_{3/2} \rightarrow$ 3d peak position for a series of organic carboxylate ligands.

For Cu metal, the first Cu 2p absorption peak occurs at 933.1 eV, which is ~3 eV higher than that of the first peak in Cu(II). At first glance, this is surprising because core excitation edges usually shift to a higher energy with increasing oxidation state. However, the 3d band is full in metallic copper ($[Ar]4s^1 3d^{10}$) and thus the 2p → 3d transition is forbidden. The first peak in Cu(0) is the $2p_{3/2} \rightarrow$ 4s transition. The first Cu 2p absorption peak for Cu(I) essentially coincides with that of Cu metal, but it is significantly narrower and more intense. The Cu 3d band is also filled in Cu(I) ($[Ar]4s^0 3d^{10}$); thus, the onset peak in Cu(I) is also assigned to Cu 2p → 4s transitions. The Cu 2p → 4s transition intensity is larger in Cu(I) than Cu(0) due to the lower ground state occupancy of the 4s

TABLE I. Energies of characteristic features in the Cu 2p spectra of Cu(0), Cu(I), and Cu(II) species.

			Energy (eV)				
Compound	Chemical state	Transition	Experiment[a]	Ref. 77	Ref. 76	Ref. 83	Ref. 84
$CuCl_2$	Cu(II)	$2p_{3/2} \rightarrow$ 3d	930.6(2)	930.0(8)	931.3	...	931.3
CuCl	Cu(I)	$2p_{3/2} \rightarrow$ 4s	933.06(8)	...	933.7	...	933.4
Cu	Cu(0)	$2p_{3/2} \rightarrow$ 4s	933.1(2)	...	933.7	932.0(4)	...

[a]Peak position calibrated with the 1s → 3p transition of Ne gas (867.23 eV[85]).

level.[76,77] Due to the well-defined local structure and strong scattering power of Cu relative to O or Cl, the region between 936 and 944 eV in Cu metal shows strong multiple scattering features which provide a unique signal to differentiate Cu(0) and Cu(I). Peak C (Fig. 4) at 937.0 eV in Cu(0) was used for this purpose.

B. *In situ* monitoring of Cu electrodeposition

Figure 6(a) plots CV signals obtained in one of the *in situ* flow experiments of Cu electrodeposition and electrostripping conducted on a system of 5 mM $CuSO_4 \cdot 5H_2O$ in a 25 mM solution of $(NH_4)_2SO_4$, prepared in milli-Q water using the phase 1b *in situ* flow electrochemical STXM. As the CV scan proceeds, 3-image Cu 2p stacks are collected continuously. Figure 6(b) presents the potential-time plot, which also indicates the voltage ranges over which each of the 3-energy stacks are acquired. Figure 7(a) (Multimedia view) plots the current as a function of time for the 3-cycle CV measurement. Figure 7(b) (Multimedia view) presents selected red-green-blue (RGB) color coded composites of the component maps

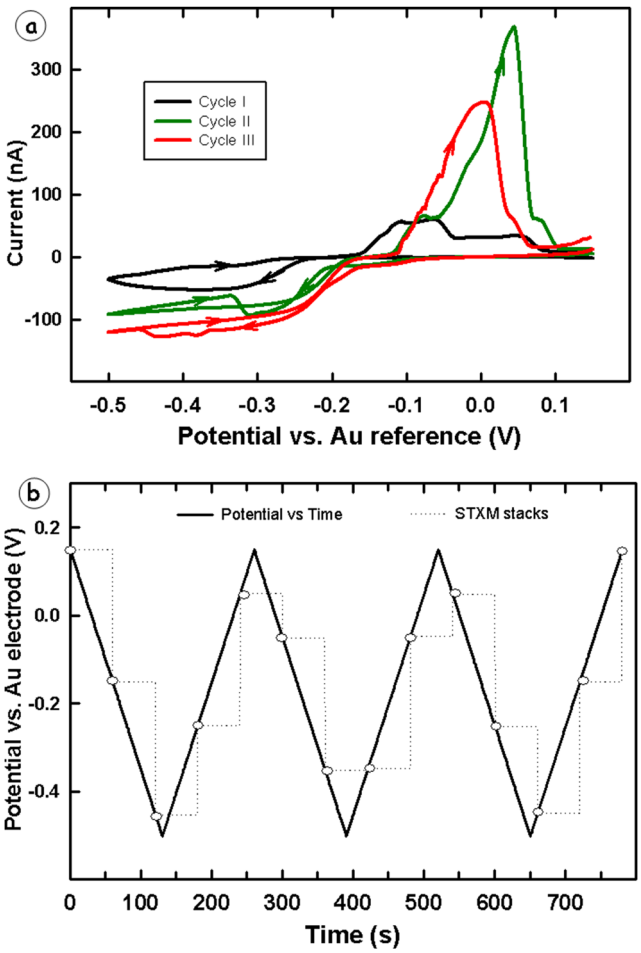

FIG. 6. (a) Cyclic voltammogram (CV) signals measured during the operation of the *in situ* flow cell with 5 mM $CuSO_4 \cdot 5H_2O$ and 25 mM $(NH_4)_2SO_4$ supporting electrolyte, obtained over 3 cycles at 5 mV/s scan rate. (b) V(t) curve for this study. The start times (o) and ranges (dotted lines) of time/potential at which each 3-energy stack was measured are indicated.

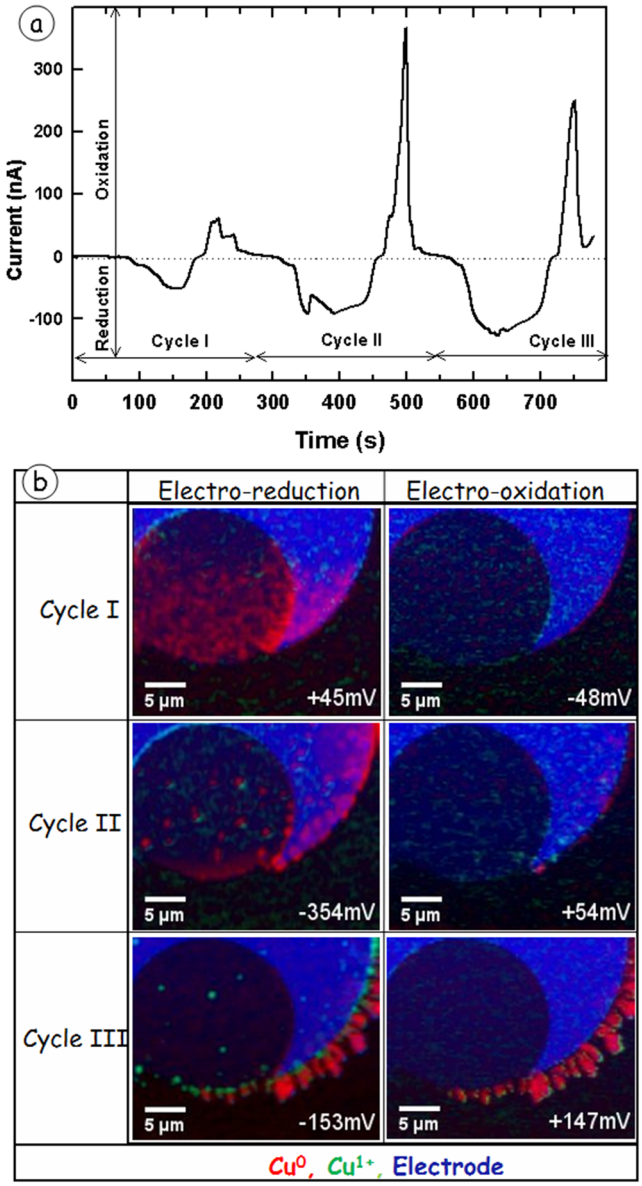

FIG. 7. (a) I(t) curve for the 3-cycle CV scan. (b) Frames from the *in situ* movie generated during the scan are shown in Multimedia view. Alternating Cu electro-deposition and electro-stripping causes the observed changes in amounts of Cu(0) (red) at the edge of the working electrode (blue) with detectable amounts of Cu(I) (green) in the electro-reduction half cycle. Multimedia view: https://doi.org/10.1063/1.5023288.2

corresponding to the peak electrodeposition and electro-stripping at each cycle. Figure 7(b) (Multimedia view)present the changes in the amounts and spatial distributions of Cu(0) and Cu(I) species during the *in situ* experiment. The movie presents the alternating deposition and stripping cycles monitored *in situ* during the cyclic voltammetric scan. The movie was constructed from frames from a single *in situ* STXM study. To improve the viewability, additional images were generated by linearly interpolating the results of each stack measurement between consecutive frames. The interpolation created 1 frame every 1.8 s from the 13 frames (stacks) acquired experimentally. Each stack took ~60 s to record and averages electrochemical changes over that period, which spans a potential range of 300 mV [see STXM stack time lines

in Fig. 6(b)]. The potentials indicated in Fig. 7(b) (Multimedia view) are the mean potential of the WE relative to the RE over the 60 s time.

The shape of the current response in the CV cycles [Fig. 7(a) (Multimedia view)] is typical for diffusion-limited electro-deposition and electro-stripping of Cu species.[46] At +0.15 V, the start value of the potential scan, the current is very small. When the potential has dropped to −0.2 V, the charge required to overcome the Helmholtz double layer charge at the electrode surface has been achieved. This is followed by a peak in the reduction current at ca. −0.31 V versus Au reference, which is similar to the reduction peak potential reported in *in situ* TEM studies of the same system.[46] Subsequently, upon reversing the direction of the potential scan at −0.5 V, the current is low until a potential of ca. +0.05 V is reached, at which point a peak in the oxidation current is observed. Another interesting observation from the CV curve is the potential of the crossover of the anodic and cathodic sections of the CV curves. This is due to the use of a Au electrode, which has an entirely different microstructure compared to copper metal, causing a crystallographic substrate-metal misfit.[78] This is also why the observed reduction potentials are larger than the standard reduction potentials of copper.

The observation of oxidation and reduction features in the CV curve can be correlated with the RGB maps in Fig. 7(b) (Multimedia view) as follows. During cycle I of the CV, the frame corresponding to the first observed electrodeposition is recorded over the potential range from +195 to −105 mV. The first electro-stripping is observed on the positive scan direction from −200 to +100 mV. In the first cycle, the charge applied is used mainly for double layer charging, nucleation, and initial growth of Cu islands, followed by stripping. Small traces of Cu metal after stripping indicate a certain extent of irreversibility in the diffusion-controlled deposition and stripping of Cu. During cycle II, the electro-deposition occurs at more negative potentials (−200 to −500 mV) while the electro-stripping occurs at similar potentials (−200 to +100 mV). The deposition that occurs in cycle II is likely facilitated by the presence of pre-deposited Cu providing more defects/active sites for the induced growth of the deposits. In the third cycle, extensive further deposition occurs in the reduction half-cycle, but many of the electrodeposited dendritic Cu structures lose electrical contact with the WE and thus are not oxidized in the stripping potential range. The amount of Cu(I) steadily increases throughout the 3-cycle process. Further insights into the reversibility of the Cu electrochemical system at these conditions are given in the next section.

C. Quantitation of *in situ* electrochemical STXM data

The integrated amount of the Cu(0) and Cu(I) species at each point in the 3 cycles was determined from the quantitative component maps. Masks (1/0 pixel maps) were generated from the quantitative component maps for Cu(0) and Cu(I) by setting a thickness threshold of 5 nm. The multiplication of the full component map by the mask results in maps of Cu(0)-rich and Cu(I)-rich areas. Averaging the non-zero pixels in the masked component maps gives an average value of the thickness of the Cu(0) or Cu(I) material as well as the area of the non-zero pixels. The uncertainty in the average values was estimated by repeating a similar procedure of averaging thickness data and using the standard deviation of three repeats as an error estimate. The mean thickness and area information were used to compute the quantity, in nanograms (ng) of each component, through conventional mass-density calculations using standard densities.

Based on the quantitative data on amounts of Cu(0) and Cu(I) species in the *in situ* movie (Fig. 3) (Multimedia view), it is noted that significant deposition and stripping of Cu(I) develops only in the 3rd cycle, which unfortunately could not be used to study the quantitative reversibility of the electrodeposition system due to the electrical disconnect of dendrites. Instead, a detailed account of the reversibility of the system is presented in terms of Cu(0) deposition and stripping. Figure 8(a) plots the amount of Cu(0) deposited with respect to time during the potential sweep experiment. The amounts of Cu(0) at the end of each reduction and oxidation peak were used to estimate the stripping efficiency at the end of each CV cycle [Fig. 8(b)]. Based on the *in situ* movie (Fig. 3) (Multimedia view) and the stripping efficiency data, it is noted that

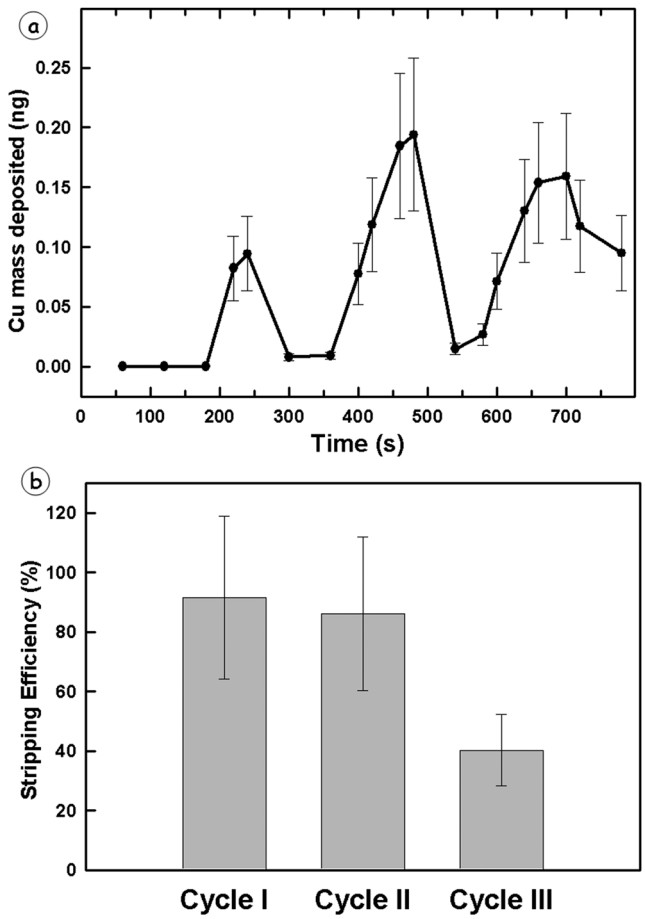

FIG. 8. (a) Quantitation of the amount of Cu(0) deposited as a function of time during the CV scan and (b) plot indicating the reversibility of the Cu electrochemical system—a fully reversible system would have a stripping efficiency of 100%. The decreasing stripping efficiency is related to irreversible deposition due to dendritic growth [see Fig. 6(b)] and loss of electrical contact.

conformal and near-uniform films at the beginning of the CV experiment turn into rounded dendrites in the 2nd cycle at the current densities that were passed through the WE. Upon reversing the current, parts of the dendrites are left behind in the electrolyte region, leading to deterioration in the stripping efficiency during the CV experiment.

V. DISCUSSION

Related to the requirement of pure Cu metal deposition for semiconductor interconnects,[1] electrodeposition at current densities greater than 45 A/m^2 as occurred in the 2nd and 3rd cycles will lead to Cu(I) contamination and dendritic growth of Cu(0) deposits. Neither phenomenon is desirable. Thus, a pulse-reversal current deposition at the current densities observed in the 1st cycle (15–25 A/m^2) is advisable for Cu deposition in order to minimize Cu(I) contamination and dendritic growth of Cu(0) deposits.

Despite successful demonstrations of *in situ* flow electrochemistry, there are significant limitations of the present phase 1b device. These include the following:

- Small operating window of flow rates owing to the small cell geometry, which limits higher flow rates. It is probably also unsuitable for applications requiring a turbulent flow, such as those used in Zn redox flow batteries. Systems which can adjust the gap between windows, such as that developed at UVSOR[80] would be able to work at a higher rate or turbulent flow.
- Lack of a system to vent gases evolved in electrochemical reactions. This precludes the use of the device for studies of processes involving gas evolution, such as hydrogen and chlorine electrochemical generation technologies. There are plans to extend the present device to include one or two additional ports for gas introduction and exhaust.
- Successful *in situ* electrochemical STXM studies requires prolonged exposure of the sample to soft X-rays at the absorption edge of the material of interest, which makes this technique not suitable for materials highly sensitive to X-ray exposure. In addition, the radiolysis of aqueous electrolytes is known to lead to solvated electrons, radicals (H, OH), ions, and gases[79] which can lead to significant and unintended modifications of the chemistry. This issue has been identified previously in the field of *in situ* electrochemical TEM, where the problem is significantly more severe.
- The current density distribution for this 3-electrode geometry is such that there is a higher current density along edges of the electrodes which leads to excess deposition at edges and non-conformal deposition over the electrode surface. In future, modeling of the fields for different electrode geometries could lead to a system with less impact of electrode edges on the outcome of the electrochemistry.
- Limited parameter ranges: a flow rate of 50 μl/h (twice that used) caused leaks and occasional window breakage. Pressure head has to be very small, less than 0.01 bar differential between the inlet and outlet.
- Finite detection limits, which are set by the use of transmission detection. Typically one cannot detect less than 1% of a component, except in cases of very strong signals [such as the Cu $2p_{3/2} \rightarrow 3p$ transition in Cu(II)] where STXM is probably capable of detecting 0.1%.
- Limited area for study. Due to scan speed limitations, it is not practical to track electrochemical events at high spatial resolution across the entire working electrode. However, smaller areas can be recorded more quickly, and tracking changes at a single position at 1 energy or with short lines can be done with sub-second sampling, as has been shown previously.[29] Even with the slow rate of acquisition used in this work, the ability to monitor changes in chemical states over space, time, and applied potential provides added-value relative to other *in situ* and *operando* electrochemical spectromicroscopy methods.

Overcoming the above limitations is not within the scope of the current generation of devices. We consider these as a motivation toward the evolution of "Phase 2" of the *in situ* electrochemical STXM. To stress its advantages, the current phase 1b device is a custom made and cost-efficient system compared to commercial devices such as the Hummingbird Scientific's X-ray liquid holder.[81] This allows users the possibility to explore modifications to the electrode surface, such as:

- Deposition of battery electrode materials and use of non-aqueous electrolytes.
- In-jet printing of the PEM-FC catalyst, which is a target of our future studies.
- Drop-casting of mineral-bacteria complexes at the working electrode, which has been attempted by Martin Obst and his co-workers.

Further improvements in the device fabrication and assembly techniques of the phase 1b instrumentation, which will lead to a more reliable system for *in situ* flow electrochemical STXM studies, include the following:

- Use of an epoxy sealant at the edges of the sandwich in order to eliminate leaks due to pressure gradients in the flow channel. If done carefully, it will be possible to operate the device in vacuum, which is now a requirement at some STXM microscopes.
- Use of a calibrated torque wrench to reliably assemble the bias and keeper piece without cracking the silicon chips or breaking the SiNx windows.
- Use of chip-to-chip sealing to directly bond the two chips, thereby forming a vacuum compatible flow cell. An attempt to use the phase 1b instrumentation with pumping the STXM tank resulted in a significant failure. Due to this incident, operating the phase 1b device with the STXM tank under vacuum is not recommended. The direct bonding approach should provide reliable, high vacuum operation for *in situ* electrochemical studies, and the electrode surface can be modified by *in situ* metal deposition. However, a major limitation of the direct bonding approach relative to the initial motivation for this instrument is that it would not be possible

to introduce solids, such as microtomed polymer thin films, as electrodes, or for the end-user to directly modify electrodes, such as to inkjet print fuel cell cathode layers.

VI. SUMMARY

An electrochemical flow cell for *in situ* scanning transmission X-ray microscopy studies, consisting of silicon microfabricated chips and a 3D printed holder, was developed and first results were presented. The silicon wafer devices, equipped with X-ray transparent Si_3N_4 membrane windows, functionalized chip surfaces, and deposited electrodes, provide a budget friendly platform to carry out studies on electrochemical systems at ~25 nm spatial resolution. An operational procedure for successful setup and the use of the technique was provided and results were presented from a sample study of Cu electrodeposition and electrostripping. The system should find applications in diverse fields including but not limited to fuel cell optimization, battery technology, corrosion protection, bio-sensors, studies of environmental redox processes, etc. A noteworthy observation is the irreversible formation of dendrites. The dendritic growth of Cu in the fabrication of semiconductor interconnects can lead to device failure.[82] The *in situ* electrochemical STXM technique described here may be a useful tool for the optimization of electrochemical deposition processes and for understanding failure mechanisms.

ACKNOWLEDGMENTS

Research was supported by NSERC (Canada), CaRPE-FC, and the Canada Research Chairs program. We thank Chithra Karunakaran, Jigang Zhou, and Yingshen Lu for beamline support. Research was performed using the ambient STXM at the Canadian Light Source beamline 10ID1 and STXMs on the 5.3.2.2 and 11.0.2 beamlines at the Advanced Light Source (ALS). CLS is supported by CFI, NSERC, CIHR, NRC, and the University of Saskatchewan. The ALS is supported by the Director, Office of Energy Research, Office of Basic Energy Sciences, Materials Sciences Division of the U.S. Department of Energy, under Contract No. DE-AC02-05CH11231. M.O. contributions were supported by DFG Grant Nos. OB362/1-1 and OB 362/4-1.

[1] R. Rosenberg, D. C. Edelstein, A. C.-K. Hu, and K. P. Rodbell, Annu. Rev. Mater. Sci. **30**, 229 (2000).
[2] D. Grieshaber, R. MacKenzie, J. Vörös, and E. Reimhult, Sensors **8**, 1400 (2008).
[3] D. Wei, P. Andrew, and T. Ryhänen, J. Chem. Technol. Biotechnol. **85**, 1547 (2010).
[4] A. Kirubakaran, S. Jain, and R. K. Nema, Renewable Sustainable Energy Rev. **13**, 2430 (2009).
[5] X. Luo, J. Wang, M. Dooner, and J. Clarke, Appl. Energy **137**, 511 (2015).
[6] J. W. Dini and D. D. Snyder, *Modern Electroplating* (John Wiley & Sons, Inc., 2010).
[7] D. Lee, M. F. Rubner, and R. E. Cohen, Nano Lett. **6**, 2305 (2006).
[8] S. Guo and S. Dong, TrAC, Trends Anal. Chem. **28**, 96 (2009).
[9] C. T. J. Low, R. G. A. Wills, and F. C. Walsh, Surf. Coat. Technol. **201**, 371 (2006).
[10] M. Armand, F. Endres, D. R. MacFarlane, H. Ohno, and B. Scrosati, Nat. Mater. **8**, 621 (2009).
[11] A. Bard and L. Faulkner, *Electrochemical Methods: Fundamentals and Applications* (John Wiley & Sons, Inc., 2001).
[12] G. Herzog and V. Beni, Anal. Chim. Acta **769**, 10 (2013).
[13] C. M. Li and W. Hu, J. Electroanal. Chem. **688**, 20 (2013).
[14] M. C. Henstridge and R. G. Compton, Chem. Rec. **12**, 63 (2012).
[15] B. Liu and M. V. Mirkin, Electroanalysis **12**, 1433 (2000).
[16] C. Wei, G. Wu, S. Yang, and Q. Liu, Sci. Rep. **6**, 34779 (2016).
[17] E. Lombi, G. M. Hettiarachchi, and K. G. Scheckel, J. Environ. Qual. **40**, 659 (2011).
[18] E. R. White, S. B. Singer, V. Augustyn, W. A. Hubbard, M. Mecklenburg, B. Dunn, and B. C. Regan, ACS Nano **6**, 6308 (2012).
[19] R. E. Gyurcsányi and E. Lindner, Anal. Chem. **77**, 2132 (2005).
[20] R. J. Gale, *Spectroelectrochemistry Theory and Practice* (Springer Verlag, 2012).
[21] E. M. Genies, G. Bidan, and A. F. Diaz, J. Electroanal. Chem. Interfacial Electrochem. **149**, 101 (1983).
[22] H. Kato, O. Nishikawa, T. Matsui, S. Honma, and H. Kokado, J. Phys. Chem. **95**, 6014 (1991).
[23] R. G. Compton and A. M. Waller, J. Electroanal. Chem. Interfacial Electrochem. **195**, 289 (1985).
[24] M. Lapkowski and E. M. Geniés, J. Electroanal. Chem. Interfacial Electrochem. **279**, 157 (1990).
[25] S. J. Randolph, A. Botman, and M. Toth, RSC Adv. **3**, 20016 (2013).
[26] S. Kaya, H. Ogasawara, L.-Å. Näslund, J.-O. Forsell, H. S. Casalongue, D. J. Miller, and A. Nilsson, Catal. Today **205**, 101 (2013).
[27] A. P. Hitchcock, "Soft x-ray imaging and spectromicroscopy," in *Volume II of Handbook of Nanoscopy*, edited by G. Van Tendeloo, D. Van Dyck, and S. J. Pennycook (Wiley-VCH Verlag GmbH & Co. KGaA, 2012), Chap. 22.
[28] J. Stöhr, *NEXAFS Spectroscopy* (Springer, 1992).
[29] D. Guay, J. Stewart-Ornstein, X. Zhang, and A. P. Hitchcock, Anal. Chem. **77**, 3479 (2005).
[30] B. Bozzini, L. D'Urzo, A. Gianoncelli, B. Kaulich, M. Kiskinova, M. Prasciolu, and A. Tadjeddine, Electrochem. Commun. **10**, 1680 (2008).
[31] B. Bozzini, A. Gianoncelli, P. Bocchetta, S. Dal Zilio, and G. Kourousias, Anal. Chem. **86**, 664 (2014).
[32] B. Bozzini, G. Kourousias, A. Gianoncelli, M. W. M. Jones, G. Van Riessen, and M. Kiskanova, J. Electron Spectrosc. Relat. Phenom. **220**, 147 (2017).
[33] J. Lim, Y. Li, D. H. Alsem, H. So, S. C. Lee, P. Bai, D. A. Cogswell, X. Liu, N. Jin, Y.-S. Yu, N. J. Salmon, D. A. Shapiro, M. Z. Bazant, T. Tyliszczak, and W. C. Chueh, Science **353**, 566 (2016).
[34] J. Cabana, L. Monconduit, D. Larcher, and M. R. Palacín, Adv. Mater. **22**, E170 (2010).
[35] M. M. Doeff, G. Chen, J. Cabana, T. J. Richardson, A. Mehta, M. Shirpour, H. Duncan, C. Kim, K. C. Kam, and T. Conry, J. Visualized Exp. **81**, e50594 (2013).
[36] M. Nagasaka, T. Hatsui, T. Horigome, Y. Hamamura, and N. Kosugi, J. Electron Spectrosc. Relat. Phenom. **177**, 130 (2010).
[37] S. Wu, Z. Shi, J. Lipkowski, A. P. Hitchcock, and T. Tyliszczak, J. Phys. Chem. B **101**, 10310 (1997).
[38] A. Adriaens and M. Dowsett, Acc. Chem. Res. **43**, 927 (2010).
[39] T. S. Arthur, P. Glans, N. Singh, O. Tutusaus, K. Nie, Y. S. Liu, F. Mizuno, J. Guo, D. H. Alsem, N. J. Salmon, and R. Mohtadi, Chem. Mater. **29**, 7183 (2017).
[40] J. Wang, Y.-C. K. Chen-Wiegart, and J. Wang, Chem. Commun. **49**, 6480 (2013).
[41] H. Sugi, T. Akimoto, K. Sutoh, S. Chaen, N. Oishi, and S. Suzuki, Proc. Natl. Acad. Sci. U. S. A. **94**, 4378 (1997).
[42] P. L. Gai, Microsc. Microanal. **8**, 21 (2002).
[43] S. E. Donnelly, R. C. Birtcher, C. W. Allen, I. Morrison, K. Furuya, M. Song, K. Mitsuishi, and U. Dahmen, Science **296**, 507 (2002).
[44] M. J. Williamson, R. M. Tromp, P. M. Vereecken, R. Hull, and F. M. Ross, Nat. Mater. **2**, 532 (2003).
[45] R. R. Unocic, R. L. Sacci, G. M. Veith, N. J. Dudney, and K. L. More, Microsc. Microanal. **20**, 1506 (2014).
[46] N. M. Schneider, J. H. Park, J. M. Grogan, S. Kodambaka, D. A. Steingart, F. M. Ross, and H. H. Bau, Microsc. Microanal. **19**, 422 (2013).
[47] N. M. Schneider, J. H. Park, J. M. Grogan, S. Kodambaka, D. A. Steingart, F. M. Ross, and H. H. Bau, Microsc. Microanal. **20**, 1530 (2014).
[48] B. L. Mehdi, M. Gu, L. R. Parent, W. Xu, E. N. Nasybulin, X. Chen, R. R. Unocic, P. Xu, D. A. Welch, P. Abellan, J.-G. Zhang, J. Liu, C.-M. Wang, I. Arslan, J. Evans, and N. D. Browning, Microsc. Microanal. **20**, 484 (2014).
[49] M. E. Holtz, Y. Yu, D. Gunceler, J. Gao, R. Sundararaman, K. A. Schwarz, T. A. Arias, H. D. Abruña, and D. A. Muller, Nano Lett. **14**, 1453 (2014).

[50]H. L. Xin, J. A. Mundy, Z. Liu, R. Cabezas, R. Hovden, L. F. Kourkoutis, J. Zhang, N. P. Subramanian, R. Makharia, F. T. Wagner, and D. A. Muller, Nano Lett. **12**, 490 (2012).
[51]R. R. Unocic, R. L. Sacci, G. M. Brown, G. M. Veith, N. J. Dudney, K. L. More, F. S. Walden, D. S. Gardiner, J. Damiano, and D. P. Nackashi, Microsc. Microanal. **20**, 452 (2014).
[52]J. Grogan, N. M. Schneider, F. Ross, and H. H. Bau, J. Indian Inst. Sci. **92**, 295 (2012).
[53]E. A. Lewis, S. J. Haigh, T. J. A. Slater, Z. He, M. A. Kulzick, M. G. Burke, and N. J. Zaluzec, Chem. Commun. **50**, 10019 (2014).
[54]A. P. Hitchcock, Z. Qin, S. M. Rosendahl, V. Lee, M. Reynolds, and H. Hosseinkhannazer, AIP Conf. Proc. **1696**, 020003 (2016).
[55]A. L. D. Kilcoyne, T. Tyliszczak, W. F. Steele, S. Fakra, P. Hitchcock, K. Franck, E. Anderson, B. Harteneck, E. G. Rightor, G. E. Mitchell, A. P. Hitchcock, L. Yang, T. Warwick, and H. Ade, J. Synchrotron Radiat. **10**, 125 (2003).
[56]B. Bozzini, M. Amati, L. Gregoratti, and M. Kiskinova, Sci. Rep. **3**, 2848 (2013).
[57]R. Walczak, K. Adamski, A. Pokrzywnicka, and W. Kubicki, Procedia Eng. **168**, 1362 (2016).
[58]See http://www.idex-hs.com/fluidics/fluidic-connections for IDEX Health & Science, LLC.
[59]See http://www.syringepump.com/NE-1000.php for New Era Syringe Pump.
[60]See http://www.somalcanada.com for P. Somal watches.
[61]See http://www.ivium.nl for Ivium potentiostats.
[62]K. V. Kaznatcheev, C. Karunakaran, U. D. Lanke, S. G. Urquhart, M. Obst, and A. P. Hitchcock, Nucl. Instrum. Methods Phys. Res., Sect. A **582**, 96 (2007).
[63]C. Jacobsen, S. Wirick, G. Flynn, and C. J. Zimba, J. Microsc. **197**, 173 (2000).
[64]A. P. Hitchcock, aXis2000 is written in Interactive Data Language (IDL). It is available free for non-commercial use from http://unicorn.mcmaster.ca/aXis2000.html; Last accessed 04 April 2018 (2016).
[65]B. L. Henke, E. M. Gullikson, and J. C. Davis, At. Data Nucl. Data Tables **54**, 181 (1993).
[66]R. Weast, *CRC Handbook of Chemistry and Physics* (Chemical Rubber Company Publishing, Boca Raton, FL, 1984), p. E110.
[67]Y. Li and P. A. Korzhavyi, Dalton Trans. **46**, 529 (2017).
[68]H. W. Richardson, *Ullmann's Encyclopedia of Industrial Chemistry* (Wiley-VCH, Weinheim, 2002).
[69]See http://www.bd.com/en-us/offerings/capabilities/syringes-and-needles for B. D. Plastic.
[70]V. Prabu, M.Sc. thesis, McMaster University, Hamilton, 2017, http://hdl.handle.net/11375/22178.
[71]H. Bruus, *Microscale Acoustofluidics* (The Royal Society of Chemistry, 2015).
[72]F. M. White, *Fluid Mechanics* (WCB/McGraw-Hill, Boston, Mass, 1999).
[73]A. I. Danilov, E. B. Molodkina, A. V. Rudnev, Y. M. Polukarov, and J. M. Feliu, Electrochim. Acta **50**, 5032 (2005).
[74]I. N. Koprinarov, A. P. Hitchcock, C. McCrory, and R. F. Childs, J. Phys. Chem. B **106**, 5358 (2002).
[75]M. Magnuson, N. Wassdahl, and J. Nordgren, Phys. Rev. B **56**, 12238 (1997).
[76]M. Grioni, J. F. van Acker, M. T. Czyżyk, and J. C. Fuggle, Phys. Rev. B **45**, 3309 (1992).
[77]C. L. Phillips, T. Z. Regier, and D. Peak, Environ. Sci. Technol. **47**, 14290 (2013).
[78]D. Pletcher, R. Greff, R. Peat, L. M. Peter, and J. Robinson, *Instrumental Methods in Electrochemistry* (Woodhead Publishing, 2010).
[79]N. M. Schneider, M. M. Norton, B. J. Mendel, J. M. Grogan, F. M. Ross, and H. H. Bau, J. Phys. Chem. C **118**, 22373 (2014).
[80]T. Ohigashi, M. Nagasaka, T. Horigome, N. Kosugi, S. M. Rosendahl, and A. P. Hitchcock, AIP Conf. Proc. **1741**, 050002 (2016).
[81]See http://hummingbirdscientific.com/products/x-ray-liquid for Hummingbird Scientific, Inc.
[82]M. Bazu and T. Bajenescu, *Failure Analysis: A Practical Guide for Manufacturers of Electronic Components and Systems* (Wiley, 2011).
[83]G. N. Greaves, P. J. Durham, G. Diakun, and P. Quinn, Nature **294**, 139 (1981).
[84]L. Tjeng, C. Chen, and S. Cheong, Phys. Rev. B **45**, 8205 (1992).
[85]C. E. Brion, S. Daviel, R. Sodhi, A. P. Hitchcock, H. C. Wolfe, and B. Crasemann, AIP Conf. Proc. **94**, 429 (1982).